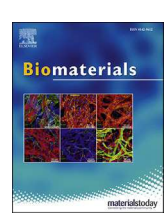


Contents lists available at ScienceDirect

Biomaterials

journal homepage: www.elsevier.com/locate/biomaterials



Leading Opinion

Detecting the functional complexities between high-density lipoprotein mimetics



Yoshitaka J. Sei ^{a, b}, Jungho Ahn ^{a, c}, Taeyoung Kim ^a, Eunjung Shin ^d, Angel J. Santiago-Lopez ^{b, e}, Seung Soon Jang ^{b, f, h}, Noo Li Jeon ^c, Young C. Jang ^{b, d, g}, YongTae Kim ^{a, b, g, h, *}

- ^a George W. Woodruff School of Mechanical Engineering, Georgia Institute of Technology, Atlanta, GA 30332, USA
- ^b Parker H. Petit Institute for Bioengineering and Bioscience, Georgia Institute of Technology, Atlanta, GA 30332, USA
- ^c School of Mechanical and Aerospace Engineering, Seoul National University, Seoul, 151-744, South Korea
- ^d School of Biological Sciences, Georgia Institute of Technology, Atlanta, GA 30332, USA
- e School of Chemical and Biomolecular Engineering, Georgia Institute of Technology, Atlanta, GA 30332, USA
- f School of Materials Science and Engineering, Georgia Institute of Technology, Atlanta, GA 30332, USA
- g Wallace H. Coulter Department of Biomedical Engineering, Georgia Institute of Technology, Atlanta, GA 30332, USA
- ^h Institute for Electronics and Nanotechnology, Georgia Institute of Technology, Atlanta, GA 30332, USA

ARTICLE INFO

Article history: Received 5 February 2018 Received in revised form 3 April 2018 Accepted 5 April 2018 Available online 6 April 2018

Keywords: Apolipoprotein A1 Microfluidics Nanoparticles ApoA1-mimetic Drug delivery

ABSTRACT

High-density lipoprotein (HDL) is a key regulator of lipid homeostasis through its native roles like reverse cholesterol transport. The reconstitution of this natural nanoparticle (NP) has become a nexus between nanomedicine and multi-disease therapies, for which a major portion of HDL functionality is attributed to its primary scaffolding protein, apolipoprotein A1 (apoA1), ApoA1-mimetic peptides were formulated as cost-effective alternatives to apoA1-based therapies; reverse-4F (r4F) is one such peptide used as part of a nanoparticle platform. While similarities between r4F- and apoA1-based HDL-mimetic nanoparticles have been identified, key functional differences native to HDL have remained undetected. In the present study, we executed a multidisciplinary approach to uncover these differences by exploring the form, function, and medical applicability of engineered HDL-mimetic NPs (eHNPs) made from r4F (eHNP-r4F) and from apoA1 (eHNP-A1). Comparative analyses of the eHNPs through computational molecular dynamics (MD), advanced microfluidic NP synthesis and screening technologies, and in vivo animal model studies extracted distinguishable eHNP characteristics: the eHNPs share identical structural and compositional characteristics with distinct differences in NP stability and organization; eHNP-A1 could more significantly stimulate anti-inflammatory responses characteristic of the scavenger receptor class B type 1 (SR-B1) mediated pathways; and eHNP-A1 could outperform eHNP-r4F in the delivery of a model hydrophobic drug to an in vivo tumor. The biomimetic microfluidic technologies and MD simulations uniquely enabled our comparative analysis through which we determined that while eHNP-r4F is a capable NP with properties mimicking natural eHNP-A1, challenges remain in reconstituting the full functionality of NPs naturally derived from humans.

© 2018 Elsevier Ltd. All rights reserved.

E-mail address: ytkim@gatech.edu (Y. Kim).

1. Introduction

High-density lipoprotein (HDL) is an endogenous nanoparticle (NP) with anti-inflammatory properties and carrier capabilities. With an average diameter of 7–17 nm, HDL naturally transitions between spherical and discoidal configurations with the encapsulation and removal of cholesterols or other hydrophobic molecules from its hydrophobic core [1]. The impact of HDL and its transitioning structure is largely attributed to the functions of its

^{*} Corresponding author. George W. Woodruff School of Mechanical Engineering, Wallace H. Coulter Department of Biomedical Engineering, Institute for Electronics and Nanotechnology (IEN), Parker H. Petit Institute for Bioengineering and Bioscience (IBB), Georgia Institute of Technology, 345 Ferst Drive (Rm 3134), Atlanta, GA 30332, USA.

primary protein component, apolipoprotein A1 (apoA1), which serves both as a scaffold to bind free lipids and cholesterols and as an agonist for anti-inflammatory processes like reverse cholesterol transport (RCT) from macrophages and the production of endothelial nitric oxide (NO) [1]. The most common receptors involved in the apoA1-stimulated regulatory processes include scavenger receptor class B type 1 (SR-B1), ATP-binding cassette transporter subfamily A member 1 (ABCA1), and ATP-binding cassette transporter subfamily G member 1 (ABCG1); while ABCA1 and ABCG1 are primarily attributed to RCT from macrophages, SR-B1 has been shown to be involved in both pathways of RCT and endothelial NO production [2]. Being a natural transporter for hydrophobic materials with the added anti-inflammatory benefits, HDL became a prime candidate for transporting therapeutic and diagnostic, or theranostic, agents for a variety of applications [3,4]. These applications have been applied to engineered NPs mimicking the form and function of HDL, allowing for the additional benefit of controlling the NP composition. Simplifying the complex lipidome and proteome of HDL to apoA1 and phospholipids, the development of HDL-mimetic NPs first started with direct proteo-lipidic self-assembly or the sodium cholate dialysis methods to reconstitute HDL (rHDL) [5], and has more recently incorporated microfluidic methods for a single-step assembly approach [6].

The engineering of HDL-mimetic NPs should involve a combination of computational and experimental approaches to comprehensively understand the form and function of the resulting NPs. For instance, the discoidal structure of HDL is often presented in a double-belt configuration, which has been commonly implemented in computational models of HDL self-assembly and is used to explain the structural stability of HDL [7–9]. Engineering HDLmimetics has also resulted in the development of many apoA1mimetic peptides for synthetic theranostic platforms to be used against diseases like cardiovascular disease (CVD), Alzheimer's disease, diabetes, and cancer [10,11]. Compared to apoA1, which has more than 240 amino acids, apoA1-mimetic peptides are not sequence homologous and are 18-22 amino acids in length to make the class-A amphipathic helical motif from the apoA1 lipid binding domain (Fig. S1) [10]. These mimetic peptides are also relatively cost-effective synthetic alternatives to apoA1, the purification and use of which requires difficult and expensive tests to ensure that human plasma (from which natural apolipoproteins are purified) is infection and endotoxin free [12]. Of the mimetic peptides studied, reverse-4F (r4F) has shown promising results in vivo in combatting the pathogenesis of atherosclerotic mouse models, and in the delivery of drug therapeutics [11,13-16]. The development of r4F was spurred by the varied properties among the 4F and r4F mimetic peptides, of which r4F was engineered to combine the bioavailability of 4F with different lipid-binding and antiinflammatory properties that were demonstrated in mouse models [13]. NPs formulated with r4F have already shown HDL-like structures and reactivity with the receptor SR-B1 for various theranostic applications [11,16]. However, a direct comparison of r4F to apoA1 in the context of NP form, function, and drug delivery potential has yet to be conducted.

The applications promised in NP therapies show broad reaches inclusive of imaging agents for targeted areas in the body and treatments for various diseases. With an extensive library of possibilities, different methods have been used to synthesize NPs based on lipids, polymers, proteins/peptides, and their combinations [17]; the most common method is to use bulk benchtop mixing to enhance NP self-assembly, or the spontaneous organization of NP precursors. A major challenge associated with this bulk synthesis technique is the resultant high batch-to-batch variation of the NP physicochemical properties. To address this challenge, microfluidic technology has brought a new synthesis strategy

presenting a continuous production platform for highly uniform NPs assembled through controlled mixing patterns (diffusive or convective means) [18], which facilitate precursor microscale interactions that were not achievable through traditional macroscale (centimeter to millimeter) benchtop synthesis techniques.

Additional critical barriers to translational studies for nanomedicine arise from the inability of conventional experimental model systems to conduct mechanistic studies of NP interactions with cells in pathophysiologically relevant microenvironments. Microfluidic technologies also offer a method through which to screen NP interactions with a biological microenvironment through in vitro microengineered physiological systems. These in vitro platforms, otherwise known as "organ-on-a-chip" systems, are capable of more accurately replicating the physiological tissue environment over traditional in vitro assays through the inclusion of key parameters needed for appropriate cellular functionality [19]. In the case of NPs delivered intravenously, studies examining the interactions between NPs and blood-vascular components are of great importance. Substantial research has presented 3D coculture systems of vascular endothelial cells (ECs) and mural cells (e.g., smooth muscle cells, pericytes, fibroblasts) with a lumen structure that improves the physiological relevance over nonlumen based models [20]. With such a platform commonly used to study endothelial responses such as permeability and angiogenesis [21,22], probing the capacity of HDL-mimetics to exert hallmark properties of HDL, such as stimulating the production of endothelial NO [23], is a critical step in their comparative analysis.

In this work, we conducted a comparative analysis between the use of apoA1 and r4F in HDL-mimetics. We first developed and implemented a novel microfluidic platform with which to synthesize engineered HDL-mimetic NPs (eHNPs) made from r4F and apoA1. Through the combined results of experimental and computational NP characterization techniques, our findings initially drew parallels across the various physical and chemical properties shared between the eHNPs including NP structure, size, stability, and composition. We then applied an innovative translational nanomedicine approach by pairing a microengineered vasculature system to screen eHNP function in vitro with a murine model to examine eHNP drug delivery to vascularized tumors in vivo. Our initial comparisons included eHNP interactions with cells that commonly interact with HDL; we then probed eHNP interactions with macrophages and ECs in the context of prevalent diseases such as CVD and cancer for the purposes of delivering incorporated theranostic agents. Analyzing the computational and experimental results unraveled distinct differences between the eHNPs that were tied to NP stability and the mimicry of hallmark HDL functions linked to the SR-B1 pathway.

2. Results and discussion

2.1. eHNPs share similarities in form, but they have distinct temporal differences

The engineering of NPs benefits from incorporating both computational and experimental methods to comprehensively understand the similarities and differences between different NP formulations. Comparisons between eHNP-A1 and eHNP-r4F made through molecular dynamics (MD) simulations showed similar discoidal structures for the self-assembled NPs (Fig. 1A). Transmission electron microscopy (TEM) micrographs also showed discoidal structures for both eHNP-A1 (Fig. 1B) and eHNP-r4F (Fig. 1C), the stacking structures of which were artifacts of the negative staining techniques in preparing the eHNPs for TEM imaging [24]. The synthesis of the eHNPs was accomplished using our new microfluidic platform that contains a micropost array to induce the

generation of microvortices that propagate down the length of the channel to increase the overall mixing efficiency of the platform (Fig. 1D). This microvortex propagation mixer (µVPM) mixed the precursor solutions more efficiently than our previous approach [6] to form eHNPs with a physiological composition with the addition of the micropost array (Fig. S2). With this increased mixing efficiency, synthesizing eHNPs with the µVPM resulted in highly reproducible and uniform sizes that were more physiologically relevant to natural HDL; the μVPM yielded particles closer to 10 nm with no lipid aggregates whereas the platform without microposts yielded NPs greater than 20 nm (Fig. 1E). Both eHNPs not only shared this physiological size when synthesized, but they also shared a physiological protein-lipid composition [25]; eHNP-A1 and eHNP-r4F, with average diameters of 10.1 and 11.7 nm respectively (Fig. 1F), both had a composition of 65% protein and 35% lipid (Fig. 1G). However, in terms of size stability, eHNP-A1 was more stable over the course of a week compared to eHNP-r4F (Fig. 1H). The lower size stability of eHNP-r4F may be attributed to the aggregation of eHNP-r4F over time, which is consistent with MD simulations (Fig. 11). The tendency of eHNP-r4F to aggregate may be due to the shorter 18 amino acid peptide length compared to the 240 + amino acids of apoA1. The impact of this difference is shown in the configuration of the scaffolding proteins in the MD simulations; eHNP-A1 consisted of two apoA1 proteins horizontally wrapped around the perimeter of the particle, whereas the smaller r4F peptides in eHNP-r4F were more vertically aligned around the perimeter of the particle. The shorter length of the peptides may facilitate a more dynamic exchange of lipids and peptides between particles that can cause particle aggregation (Video S1).

Supplementary video related to this article can be found at https://doi.org/10.1016/j.biomaterials.2018.04.011.

2.2. eHNP reactivity is shared with macrophages, but not with ECs

With natural HDLs most notably interacting with macrophages and ECs [1], we examined eHNP interactions with these cell types to compare the bioreactivity of eHNP-A1 and eHNP-r4F. Both eHNP-A1 and eHNP-r4F were taken up by J774a.1 macrophages to a similar extent (Fig. 2A and B), however eHNP-A1 induced 15% more cholesterol efflux compared to that of eHNP-r4F (Fig. 2C). Competition assays for endothelial and macrophage uptake of eHNP-A1 and eHNP-r4F also showed distinct difference between these 2 cell types (Fig. 2D); while J774a.1 macrophages showed a gradual decrease in uptake of rhodamine-labeled eHNP-r4F with the introduction of eHNP-A1 (Fig. 2E), human umbilical vein ECs (HUVECs) showed more than a 2-fold decrease in eHNP-r4F uptake when adding an amount of eHNP-A1 equivalent to just half the amount of eHNP-r4F (Fig. 2F). While ECs and macrophages share certain HDL receptors such as SR-B1, ABCA1, and ABCG1, macrophages express more scavenger receptors, such as scavenger receptor class A (SR-A) [2], that allow macrophages to exhibit uptake characteristics that are less selective than those of ECs. This lack of selectivity may contribute to the lack of retardation in the J774a.1 uptake of eHNP-r4F with the addition of eHNP-A1. In addition, the differences between eHNP reactivity may be tied specifically to the receptor SR-B1 as seen with the differences in the cholesterol efflux measurements (Fig. 2C). Although the amino acid sequences between murine and human SR-B1 are 80% homologous, it should be noted that both murine and human models are appropriate for studying human lipoproteins [26,27]. Since inhibition of SR-B1 in ECs does not necessarily completely inhibit the uptake of eHNPs due to redundant HDL uptake pathways [28], we determined it was necessary to examine hallmark endothelial responses to HDL that are classically stimulated through SR-B1 triggered pathways: the production of endothelial NO and its downstream antiinflammatory effects [23].

2.3. Anti-inflammatory endothelial responses are more prominent with eHNP-A1

To further explore the preferential endothelial uptake of eHNP-A1 over eHNP-r4F, we used a microengineered vascular system (Fig. 3A) to measure 2 hallmark markers to quantify endothelial inflammation: the levels of endothelial NO production and the expression of intercellular adhesion molecule 1 (ICAM-1) [21]. While the responses of the microvascular network to the eHNPs were similar across all measurements for both eHNP-A1 and eHNPr4F, the responses were more underscored in the cases of eHNP-A1 exposure. Both eHNPs were able to significantly stimulate endothelial NO synthase (eNOS) and promote NO production, however eHNP-A1 elicited more than double the NO levels compared to the levels eHNP-r4F stimulated (Fig. 3B). A primary marker of the endothelial inflammatory process is with the expression of surface adhesion proteins; endothelial cells activated through mechanochemical stimuli such as oscillatory shear stress or inflammatory cytokines like tumor necrosis factor α (TNF- α) express several adhesion proteins, including vascular cell adhesion molecule (VCAM-1), ICAM-1, and E-selectin [1]. The ability of HDL to inhibit cytokine-induced adhesion molecule expression has been demonstrated in the protective function against the development of atherosclerosis [29]. As seen with apoA1-based reconstituted HDLs (rHDL), both eHNPs did not trigger ICAM-1 expression (Fig. 3C) and were able to significantly reduce ICAM-1 levels induced with TNF- α stimulation (Fig. 3D) [30.31]. In line with the magnified effects of eHNP-A1 on NO production however, the reduction of ICAM- 1 was more than twice as prominent with eHNP-A1. These results are consistent with the competition assay (Fig. 2F) in that HUVECs responded more preferentially in the uptake of eHNP-A1 over eHNP-r4F. While both eHNPs could trigger SR-B1 related processes in ECs, eHNP-A1 outperformed eHNP-r4F in the magnitude to which these processes were stimulated.

2.4. DOX delivery to HL-60 is facilitated with eHNPs.

The use of HDL and HDL-mimetics for therapeutic and diagnostic multi-disease applications is widely being explored due to its natural role as a stable transport vehicle for hydrophobic materials through the body [3,16]. In the case of chemotherapeutics, patient treatments employing anthracyclines have been connected to cardiovascular side effects such as acute ischemic heart disease that are typically a result of atherosclerosis [32]. With the known cardioprotective properties of apoA1 and HDL, we examined the drug delivery potential of eHNP-A1 and eHNP-r4F in the context of delivering anthracyclines. As a proof of concept for this notion, we incorporated a widely used anthracycline cancer drug, doxorubicin hydrochloride (DOX), into the eHNPs for which the resulting size distributions interestingly yielded similar peaks at 40 nm when adding equal initial amounts of DOX to the synthesis of both eHNP types (Fig. 4A). Again, it is interesting that eHNP-r4F-DOX had the same size as eHNP-A1-DOX that uses a 10× larger scaffolding protein to incorporate this model drug. To confirm the presence of DOX in our eHNPs, we found that eHNP-A1-DOX had an improved loading concentration and encapsulation efficiency over eHNP-r4F-DOX with efficiencies of 1.5% and 0.5% respectively (Fig. 4B and C); the encapsulation efficiency, without additional conjugation between drugs and NPs, was comparable to values reported by other studies for HDL platforms used for drug encapsulation [4]. The discrepancy in DOX incorporation between eHNP-A1-DOX and eHNP-r4F-DOX may be a result of the weaker stabilizing intermolecular forces of r4F than those available to apoA1 [9]; this

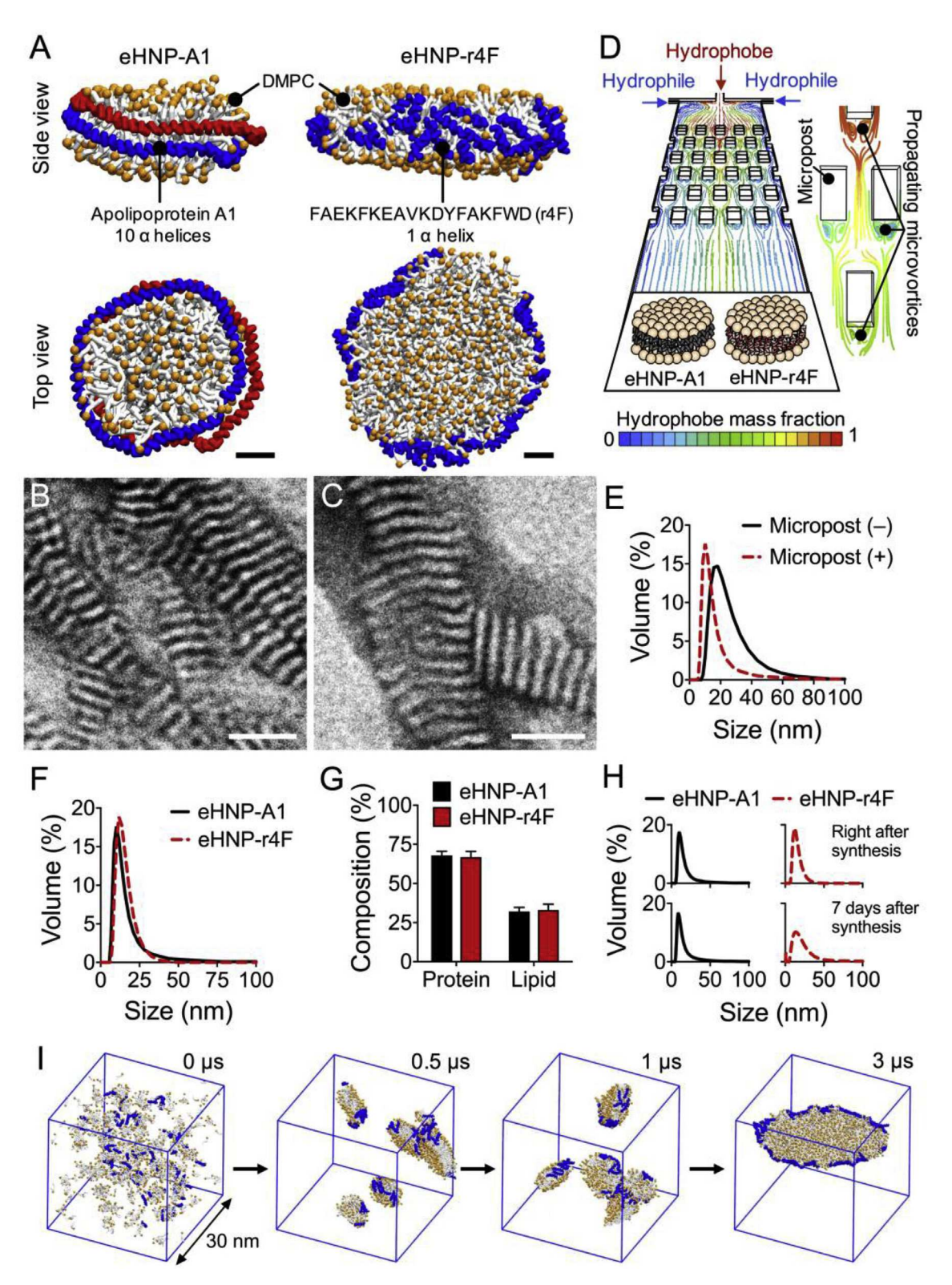


Fig. 1. Comparison of eHNPs made from apoA1 or r4F. (A) Molecular dynamics simulations show that 2.3 kDa peptide r4F self-assembles with lipids to produce discoidal eHNPs similar to those made with the 28 kDa apoA1 (scale bar is 2.5 nm). (B, C) TEM images of the synthesized eHNP-A1 (B) and eHNP-r4F (C) particles (scale bar is 25 nm). (D) A microvortex propagation mixer was engineered for the enhanced assembly of the NPs. (E) DLS size distribution of eHNPs synthesized with (+) and without (-) microposts. (F) DLS size distributions of the produced eHNPs. (G) Protein/lipid compositions of the produced eHNPs (n = 3). (H) Stability of the produced eHNPs at 4 °C after 7 days post synthesis. (I) eHNP-r4F aggregation over time in a 30 nm simulation box with a trajectory of 3 μs Plotted as mean \pm SEM.

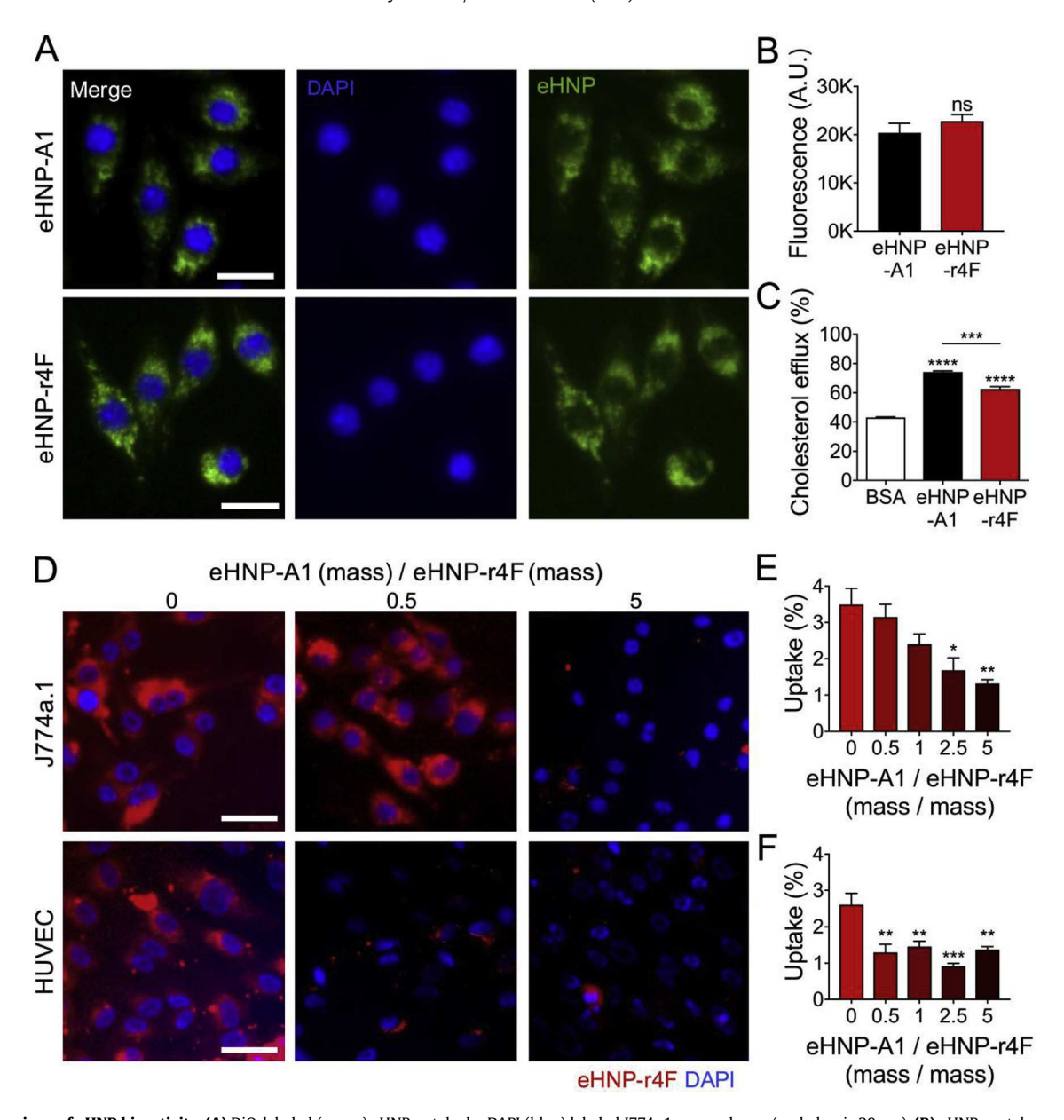


Fig. 2. Comparison of eHNP bioactivity. (**A**) DiO-labeled (green) eHNP uptake by DAPI (blue) labeled J774a.1 macrophages (scale bar is 20 μm). (**B**) eHNPs uptake quantified with fluorescence intensity (n = 4). (**C**) Cholesterol efflux with eHNPs (n = 3). (**D**) eHNP-A1 and rhodamine-DMPE labeled eHNP-r4F (red) competitive uptake by DAPI (blue) labeled J774a.1 macrophages or HUVECs (scale bar is 50 μm). (**E**, **F**) Comparison of eHNP-r4F retention by J774a.1 macrophages (**E**) and HUVECs (**F**) (n = 4). Plotted as mean ± SEM where *, and *** are for p < 0.05, 0.01, and 0.001 respectively. (For interpretation of the references to color in this figure legend, the reader is referred to the Web version of this article.)

difference in stability was also observed with drug-free eHNPs in the context of size stability (Fig. 1H).

Having diseases treated with anthracyclines in mind, we cultured acute myeloid leukemia (AML) HL-60 promyeoblasts and administered our newly synthesized eHNP-DOX with either r4F or apoA1 and an equivalent amount of DOX. The examination of the short-term (4 h) uptake of eHNP-A1-DOX and eHNP-r4F-DOX by HL-60 cells showed the eHNPs and DOX fluorescent signals colocalized primarily in the same region of the cell cytoplasm (Fig. 4D). Compared to the naked DOX case for which DOX translocated into the nucleus, our eHNPs facilitated the delivery of DOX into this cancer cell with slower translocation of DOX into the nucleus [33]. It should also be noted that the HL-60 cells treated with naked DOX and eHNP-A1-DOX exhibited more swollen nuclei than the HL-60 cells treated with eHNP-r4F-DOX and saline (Fig. 4E); nuclear swelling is a characteristic of DOX treatment [34]. This

difference in HL-60 morphology may be due to a difference in uptake between eHNP-A1-DOX and eHNP-r4F-DOX, for which we tested the cytotoxicity of the eHNPs. Over the course of a 24 h culture, we found significant drops in the HL-60 cell viability with eHNP-r4F-DOX and eHNP-A1-DOX (Fig. 4F). The cytotoxicity to the HL-60 cells proved to be more significant with eHNP-A1-DOX than with eHNP-r4F-DOX, which was consistent with the DOX-induced nuclear effects that were observed in the confocal microscopy results.

To further explore the capabilities of both eHNP-A1 and eHNP-r4F in the context of drug delivery, we studied the tumor uptake of near-infrared (NIR) dye labeled eHNPs delivering DOX in a murine xenograft tumor model of HL-60 cells. The biodistribution of the eHNPs with DOX measured using an *in vivo* imaging system (IVIS) showed a similar, yet distinct, distribution between eHNP-A1-DOX and eHNP-r4F-DOX; eHNP-A1-DOX accumulation was

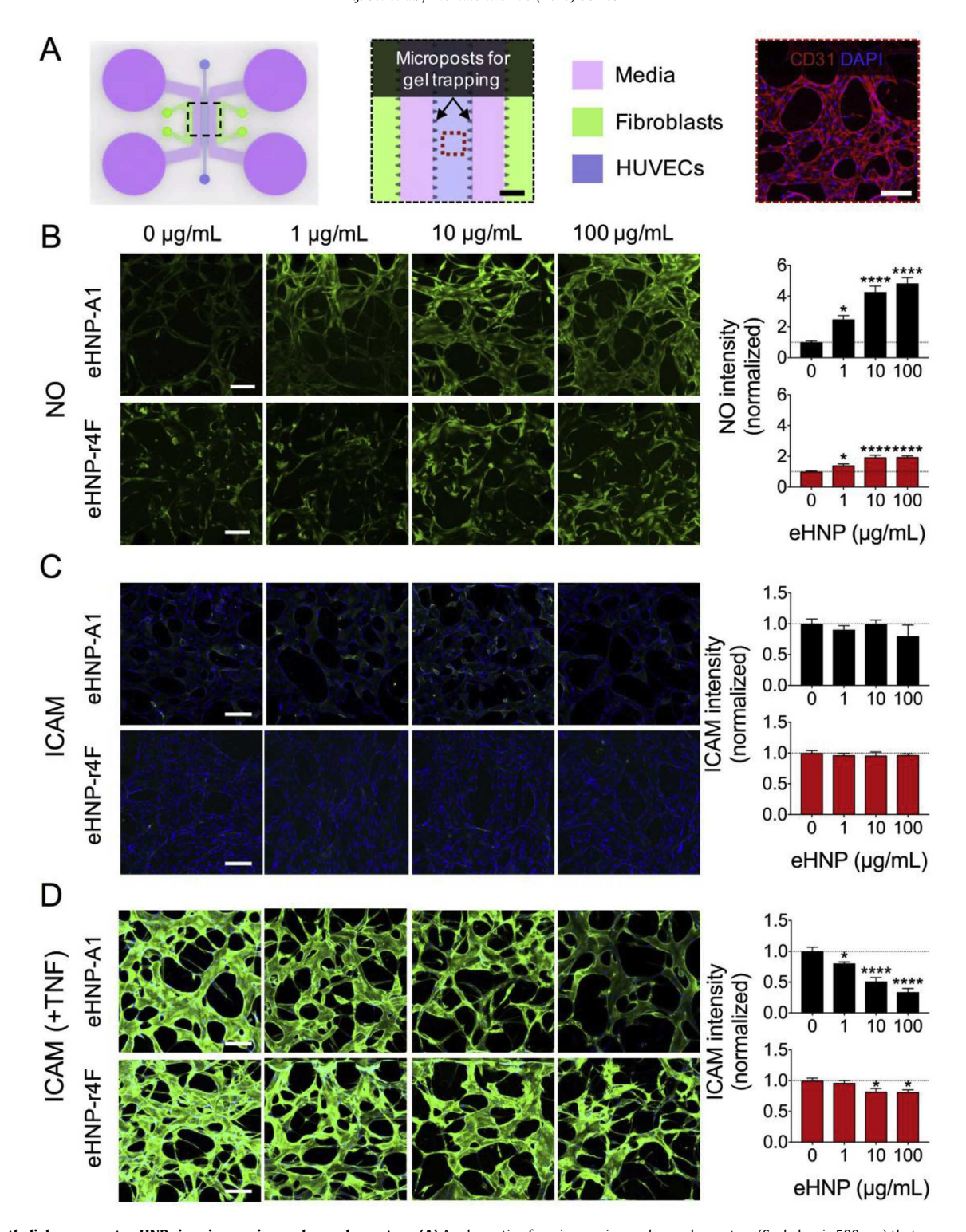


Fig. 3. Endothelial response to eHNPs in microengineered vascular system. (A) A schematic of a microengineered vascular system (Scale bar is 500 μm) that was used to screen the endothelial responses to eHNP-A1 and eHNP-r4F (Scale bar is 100 μm). **(B–D)** The endothelial responses to eHNP-A1 and eHNP-r4F were compared through nitric oxide (NO) production **(B)** and ICAM expression **(C)** with and without the presence of TNF-α **(D)** (Scale bar is 100 μm, n = 4-8). Plotted as mean \pm SEM where * and **** are for p < 0.05 and 0.0001 respectively.

significantly higher in the lung, kidney, spleen, and the tumor (Fig. 5A). Confocal imaging of the cyrosectioned tumor samples showed less delivery of DOX to the tumor site with the naked DOX treatment compared to the eHNP-DOX treatments (Fig. 5B), between which eHNP-A1-DOX treated mice showed the highest particle (Fig. 5C) and DOX (Fig. 5D) uptake by the tumor. The co-

localization of eHNP and DOX signals in the tumor sections (Fig. 5B) was also consistent with the *in vitro* results (Fig. 4D). The discrepancy between eHNP-A1 and eHNP-r4F accumulation in the tumor may be dependent on the interactions between the eHNPs and the tumor microenvironment, which has been shown to be especially important in tumor growth through processes like

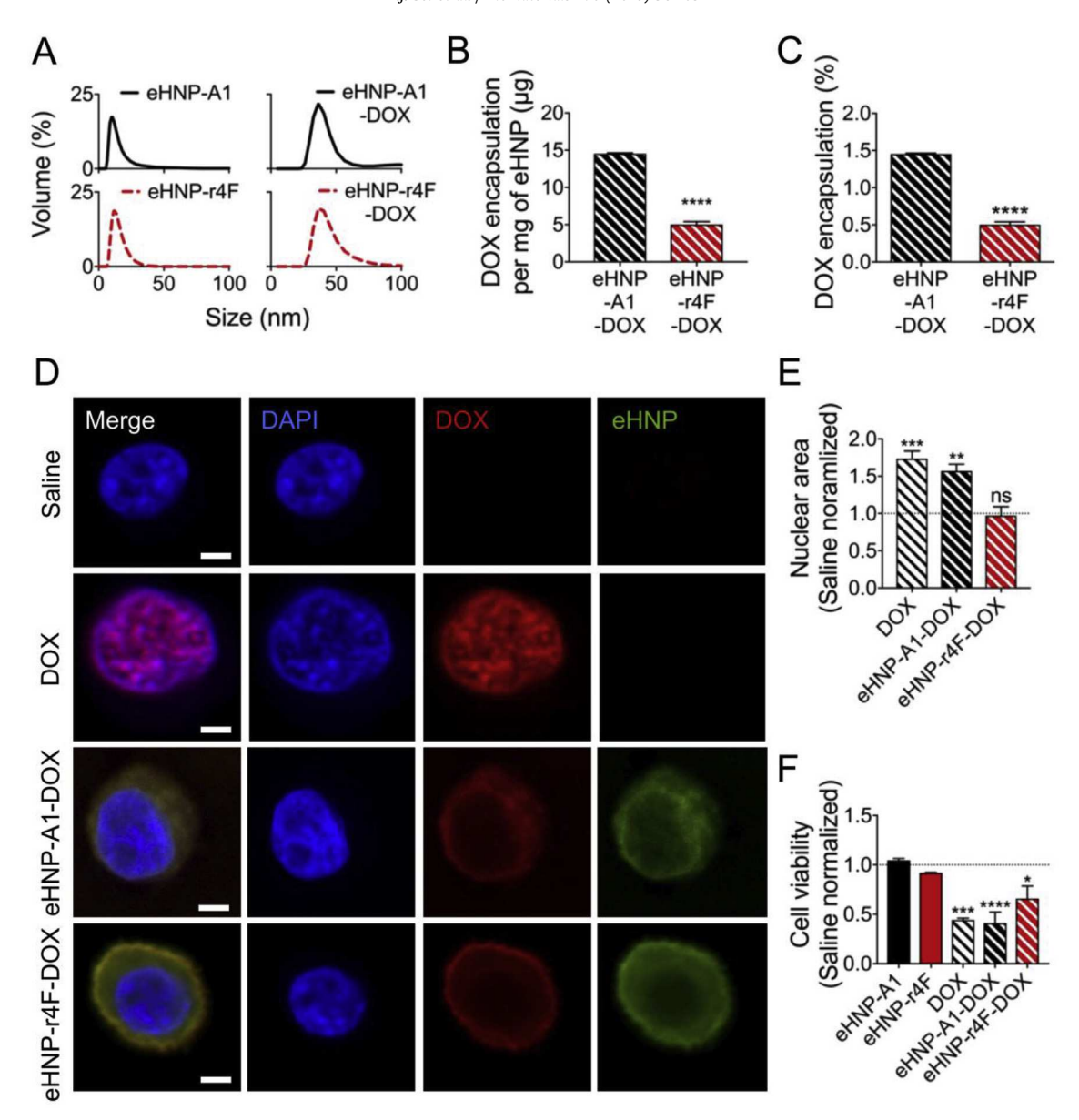


Fig. 4. Incorporating DOX into eHNPs for *in vitro* delivery. (A) DLS comparison of eHNP-A1-DOX and eHNP-r4F-DOX to eHNP-A1 and eHNP-r4F respectively. (B, C) Mass (B) and efficiency (C) of DOX loading into eHNPs (n = 3). (D) Co-localization of eHNP (green) and DOX (red) signal in HL-60 cells after 4 h of incubation (Scale bar is 5 μ m). (E) Nuclear area of HL-60 cells in response to 4 h DOX treatment (n = 5-14). (F) Cancer cell (HL-60) viability after a 24 h incubation with DOX treatment (150 ng of DOX) (n = 3). Plotted as mean \pm SEM where *, **, ***, and **** are for p < 0.05, 0.01, 0.001, and 0.0001 respectively. (For interpretation of the references to color in this figure legend, the reader is referred to the Web version of this article.)

angiogenesis [35].

Our previous work has shown that eHNP-A1 can interact with the endothelium to modulate the angiogenic process [22]. It has also been shown that the HDL-sensitive receptor SR-B1 is overexpressed in some cancers including myeloid leukemia [36]. Potential modes of SR-B1 mediated eHNP tumor retention include interactions with the tumor endothelium or the HL-60 tumor cells [2]. Thus, the differences between eHNP-A1-DOX interactions with the tumor over those of eHNP-r4F-DOX may be due to increased EC and/or HL-60 tumor cell interactions with eHNP-A1, which was already demonstrated with our *in vitro* results (Figs. 2—4). In addition, the lower stability of eHNP-r4F we found (Fig. 1H and I) may have affected the functionality through eHNP-r4F aggregation *in vivo*, resulting in a different pharmacokinetic profile in the biodistribution of eHNP-r4F-DOX. Therefore, while r4F has potential in

disease theranostics through the retention of some of apoA1's properties, the challenge remains in fully mimicking the complex functions of apoA1 and other HDL associated proteins to stimulate key functional, and potentially therapeutic, cellular responses.

3. Conclusions

HDL-mimetics offer a multitude of avenues through which to explore disease therapy. We found that eHNP-r4F was comparable to eHNP-A1 in the basic physicochemical properties: size, structure, and composition. However, eHNP-A1 could elicit cellular responses such as cholesterol efflux from macrophages and NO production in ECs at a higher level than eHNP-r4F. When further compared to eHNP-r4F, eHNP-A1 more preferentially interacted with HUVECs and significantly reduced TNF-α stimulated ICAM-1 expression in

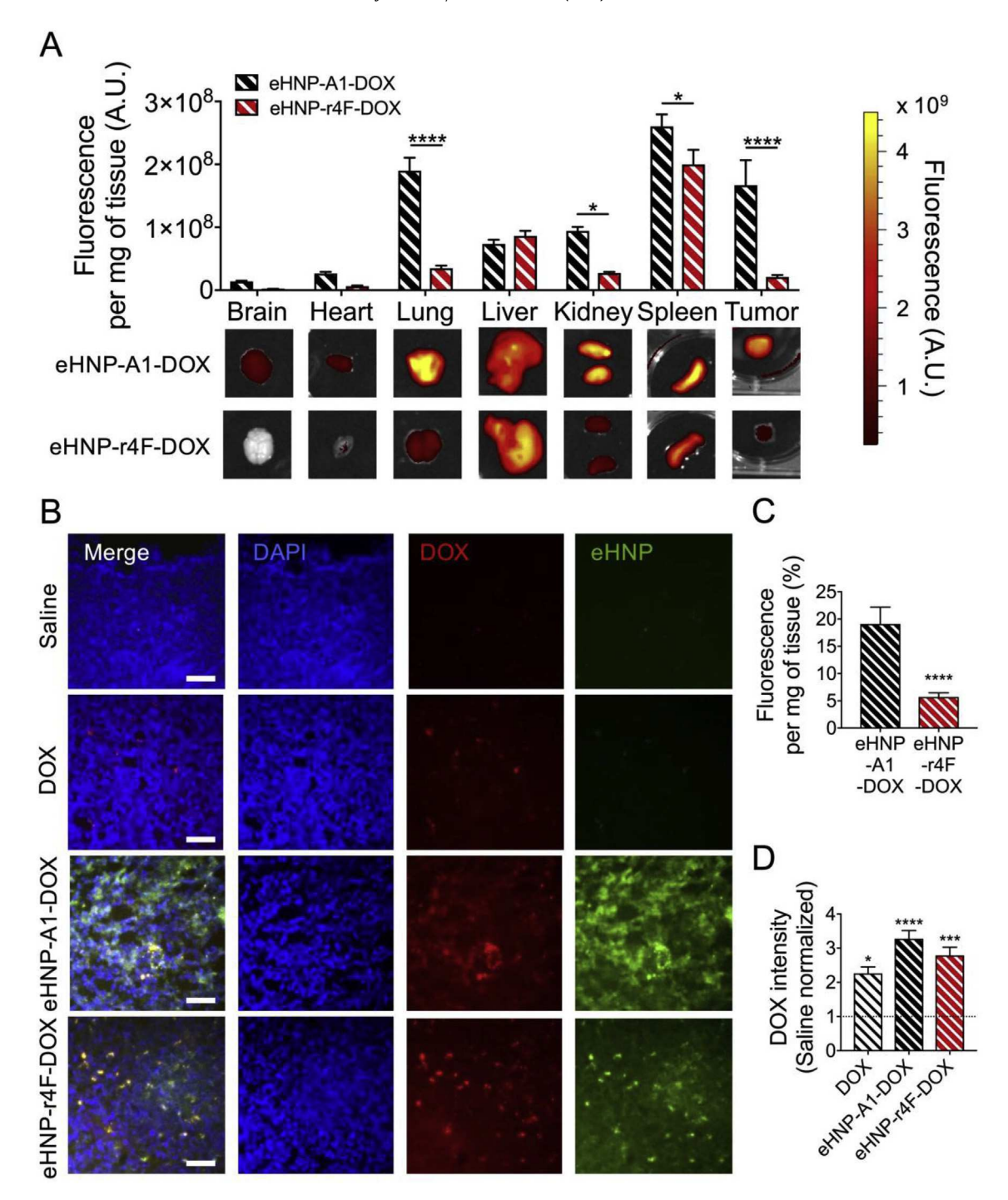


Fig. 5. eHNP-facilitated DOX delivery to xenograft tumor in a murine model. (A) Biodistribution of DiR labeled eHNPs loaded with DOX (n=7). (B) Confocal images of DiR labeled eHNPs (pseudo-colored green) and DOX (red) in DAPI (blue) labeled HL-60 tumor sections (scale bar is $50 \, \mu m$). (C) Biodistribution of eHNPs to the tumor site (n=7). (D) DOX fluorescence intensity measurements in tumors (DOX: n=4; eHNPs: n=7). Plotted as mean \pm SEM where *, ***, and **** are for p<0.05, 0.001, and 0.0001 respectively. (For interpretation of the references to color in this figure legend, the reader is referred to the Web version of this article.)

the microvascular networks. In the context of drug delivery, eHNP-A1 was also better able to incorporate and deliver DOX to the tumor cells *in vitro* and *in vivo*. However, it should be noted that eHNP-r4F was still able to deliver more doxorubicin to the tumor site over the naked DOX treatment *in vivo*. More studies are needed to elucidate the possibilities of using apoA1-based nanocarriers like our eHNPs, as the development of apoA1-mimetic peptides such as r4F may be able to serve as a cost-effective alternative to apoA1. However, it is clear from our study that apoA1 has many properties that cannot

yet be fully recapitulated using the apoA1-mimetic peptide r4F. Additional future work to be considered would be in the incorporation of other HDL-associated proteins and small molecules that modulate the functionality of HDL. By leveraging the combined insights provided from experimental and computational approaches, we may examine the functionality of eHNPs with these added components to further analyze one of the most complex and heterogeneous transporters of the body.

4 Materials and methods

4.1. eHNP synthesis materials

1,2-dimyristoyl-sn-glycero-3-phosphocholine (DMPC) and 1,2-dimyristoyl-sn-glycero-3-phosphoethanolamine-*N*-(lissamine rhodamine B sulfonyl) (Rhodamine-DMPE) were purchased from Avanti Polar Lipids, Inc. (Alabaster, AL). The near-infrared label for the eHNPs, 1,1′-Dioctadecyl-3,3,3′,3′-Tetramethylindo-tricarbocyanine lodide (DiR), was purchased from Thermo Fisher Scientific (Waltham, MA). ApoA1 from human plasma, 3,3′-dioctadecyloxacarbocyanine perchlorate (DiO), and DOX were purchased from Sigma-Aldrich Co. LLC. (St. Louis, MO). The peptide r4F was purchased from RS Synthesis, LLC. (Louisville, KY) using the sequence Ac-FAEKFKEAVKDYFAKFWD [11]. Polydimethylsiloxane (PDMS) for fabrication of the μVPM synthesis platform was made using the Sylgard 184 silicone elastomer kit purchased from Dow Corning Corporation (Auburn, MI).

4.2. Molecular dynamics simulations

The MD simulations were performed using the GROMACS software package [37]. The course grain model for the simulations was done with the MARTINI course grain force field for biomolecular systems [38]. Combining the ElneDyn elastic network model with the course grain molecular force field to maintain the secondary and tertiary structure of apoA1, we simulated the self-assembly of eHNP-A1 in a $15 \times 15 \times 15$ nm simulation box with a periodic boundary and a trajectory of 500 ns [39]. The initial conditions of the simulation involved 2 apoA1 molecules arranged in antiparallel around 160 DMPC lipids using the *insane* method for lipid bilayers [40]. Using the same boundary box size of $15 \times 15 \times 15$ nm and number of lipids, we initiated 1 µs trajectory eHNP-r4F simulations with varying protein:lipid molecular ratios based on our eHNP-A1 simulations and on past simulations using the apoA1-mimetic peptides 18A and 4F (Table S1) [41,42]. To examine the aggregation of multiple eHNP-r4F particles, we used the initial conditions of a $30 \times 30 \times 30$ nm simulation box and a protein:lipid molecular ratio of 1:16 for a trajectory of 3.5 µs [41].

4.3. μ VPM design, analysis, and fabrication

The µVPM was first conceptualized from previous platform designs using the CAD software SolidWorks from Dassault Systemes SolidWorks Corp. (Paris, France), after which we conducted computational flow studies using the solver SC/Tetra (Software Cradle Co., Ltd., Osaka, Japan) [18,43,44]. The diffusion coefficient was set for 10^{-9} m²/s for a small molecule in water at room temperature as previously determined [45]. Fabrication of prototype devices using PDMS allowed us to conduct flow visualization studies using phenol red and water imaged with an EVOS FL Auto microscope from ThermoFisher Scientific (Waltham, MA). Starting from reference inlet ratios and flowrates [6], we adjusted the flowrates of the phenol red and water while simultaneously comparing them to results yielded from the computational analysis. To evaluate the mixing efficiencies of the μVPM, we used a mixing index to compare the lipid mass fraction distributions of the channel cross sections to reduce the under-mixed lipid mass fraction at the outlet (Fig. S2) [46]. The μVPM uses three inlets and a single outlet, with a height of 100 $\mu m,$ outlet width of 2 mm, and 27 microposts with the dimensions $200 \times 400 \,\mu m$. For the device fabrication, SU-8 was spun onto 100 mm silicon wafers to a height of 100 μm before undergoing photolithography. The wafers were developed and dried before casting. PDMS was molded to the patterned silicon wafer using a 10:1 mass ratio of elastomer to curing agent before curing at $80\,^{\circ}$ C. Molded devices were then bonded to glass slides using the PDC-32G plasma cleaner from Harrick Plasma (Ithaca, NY) for 1 min.

4.4. eHNP synthesis and characterization

The synthesis conditions used for all NPs were with a Reynolds number of 50, where the flow ratio between the side streams and the center stream was 5.5:1 respectively. The NP precursor solutions included a lipid solution that was composed of DMPC with a concentration of 2.75 mg/mL in 200 proof ethanol, and a protein solution that had either apoA1 or r4F with a concentration of 0.2 mg/mL in PBS (1×, pH 7.4). Syringe pumps from Harvard Apparatus (Holliston, MA) were used to pump the solutions into the device, from which the mixed solution was collected and then triple washed with PBS using a 10,000 M.W. (30,000 M.W. when incorporating DOX or fluorescent labels) centrifugal filter from EMD Millipore Corporation (Darmstadt, Germany) at a speed of 3900 rpm for 20 min. The size distribution of the final washed sample was measured with a Zetasizer Nano ZS from Malvern Instruments (Worcestershire, United Kingdom). Protein and lipid precursor compositions between eHNP-A1 (Fig. S3) and eHNP-r4F (Fig. S4) were tuned to achieve an average size of 10 nm. Fluorescently labeled eHNPs used a modified lipid precursor solution with Rhodamine-DMPE, DiR, or DiO as 15% of the total lipid mass [14,16]. Incorporation of DOX into the eHNP was done through mixing the protein precursor solution to accommodate a 1 mg/mL solution of DOX in DMSO for a final precursor solution containing 0.2 mg/mL of both apoA1 (or r4F) and DOX. The protein-DOX precursor was then microfluidically mixed with the lipid precursor followed by a triple wash in PBS all in the same way as for when synthesizing eHNPs without DOX. eHNP-DOX samples were placed into black well, clear bottom 96 wells plates and measured using the excitation/emission wavelengths of 490/580 nm [47,48]. Samples were measured using with a Cytation 5 plate reader from BioTek (Winooski, VT). The Schiffer-Edmunson diagrams were made using the Membrane Protein Explorer (MPEx) research tool 49].

4.5. TEM preparation

Samples for TEM were prepared on nickel grids with a formwar coating from Electron Microscopy Sciences (Hatfield, PA). The NPs to be imaged were triple washed in an ammonium acetate buffer. The NPs were then loaded onto the TEM grids before they were negatively stained using a 2% phosphotungstic acid solution (PTA). The final samples were then imaged on an HT7700 TEM (Hitachi, Tokyo, Japan) at 120 kV coupled with the DigitalMicrograph camera and software suite from Gatan (Pleasanton, CA).

4.6. eHNP protein and lipid quantification

Protein quantification was done using the colorimetric Micro BCA Protein Assay kit from ThermoFisher. As per the recommendations from the instructions, SDS (1%) was added to all samples to prevent the interference of lipids on the protein measurement. Lipid quantification was done using the fluorometric Lipid Quantification Kit (neutral lipids) from Cell Biolabs, Inc. (San Diego, CA).

4.7. Cell culture

The macrophage adherent cell line J774a.1 from ATCC (Manassas, VA) was cultured in Dulbecco's Modified Eagle Medium supplemented with 1% penicillin streptomycin (PS) and 10% Fetal Bovine Serum (FBS). Human umbilical vein endothelial cells

(HUVECs) were purchased from Lonza (Basel, Switzerland), and were cultured using complete endothelial growth medium 2 (EGM-2). Normal human lung fibroblasts (LFs, Lonza) were cultured in Fibroblast Growth Medium (FGM-2, Lonza); cell passages 3–4 were used for the microengineered vascular experiments. Human promyeoblast suspension cell line HL-60 originally purchased from ATCC, cultured in complete medium consisting of Iscove's Modified Dulbecco's Medium supplemented with 20% FBS and 1% PS. Media was refreshed every 3 days.

4.8. eHNP uptake and competition assay

HUVECs and J774a.1 were cultured for 24 h in a 96-well plate before triple washing with PBS and adding culture media with rhodamine-DMPE labeled eHNP-r4F (20 $\mu g/mL$ of protein) and/or eHNP-A1 (0, 10, 20, 50, or 100 $\mu g/mL$ of protein) overnight at 37 °C. The cells were then triple washed with PBS before fixation with 4% paraformaldehyde and counter staining with DAPI. Samples were then imaged and the fluorescent intensity was analyzed using the Cytation 5 plate reader from BioTek.

4.9. Cholesterol efflux assay

J774a.1 cells were cultured in 96 well-plates (black well, clear bottom) at a density of 12,500 cells/well. Plates were cultured for 24 h before adding NBD cholesterol (ThermoFisher Scientific) overnight at a concentration of $100\,\mu\text{g/mL}$. The cells were washed the next day with PBS before incubating with 2 mg/mL fatty-acid free albumin overnight. Cells were then washed and incubated with eHNPs or BSA for 16 h. Supernatant media from each well was extracted and cells were washed with PBS. Supernatant and cell samples were measured with a Cytation 5 plate reader from BioTek using the excitation/emission wavelengths of 469/537 nm.

4.10. Cell seeding in the microengineered vascular system

A previously reported microengineered vascular system designed to probe endothelial cell responses in a 3D vascularized network was used to examine endothelial interactions with our eHNPs [21,50,51]. To fabricate the devices, SU-8 was spun onto $100\,\text{mm}$ silicon wafers to a height of $100\,\mu\text{m}$ before undergoing photolithography. The wafers were developed and dried before casting. PDMS was molded to the patterned silicon wafer using a 10:1 mass ratio of elastomer to curing agent before curing at 80 °C. Molded devices were then bonded to glass slides using the PDC-32G plasma cleaner from Harrick Plasma (Ithaca, NY) for 1 min. Fibrinogen (Sigma) was dissolved in DPBS (w/calcium and magnesium, Gibco), filter-sterilized (0.22 µm pore) and then supplemented with aprotinin (0.15 U/mL, Sigma). Fibroblasts were resuspended in the fibrinogen solution (2.5 mg/mL) at a concentration of 8×10^6 cells/mL. The cell solution was mixed with thrombin (1 U/mL, Sigma) immediately prior to injection into fibroblast channels. Following 3 min of polymerization at room temperature. The central channel was filled in the same manner as the peripheral channels; HUVECs were introduced into the gel at a concentration of 5×10^6 cells/mL instead of fibroblasts. After allowing the gels to polymerize for 3 min at room temperature, the inlet reservoirs of the cell culture medium channels were filled with EGM-2 medium, and then aspirated to fill the hydrophobic channels (Fig. S5). Following loading all four reservoirs, the microfluidic platforms were incubated at 37 °C for 5 days to allow for microvascular network formation (Fig. S6). Experiments were conducted under static conditions.

4.11. Quantifying endothelial NO production and ICAM expression

The perfusates were supplemented with L-arginine (5 mM, Sigma) and DAF-FM DA (5 µM, Molecular Probes) to support and detect the NO production by HUVECs. The levels of NO were quantified via confocal microscopy and the fluorescent intensity was analyzed with Imagel. The background fluorescence of each image was eliminated to compare NO levels between different dosage conditions, and the total fluorescence was normalized to the 0 μg/mL dosage for comparisons between eHNP-A1 and eHNP-r4F. Z-stack projections were collected to obtain an average intensity value for each chip. To compare the effect of the eHNPs on ICAM-1 expression, each microvascular network was pre-incubated with each dosage of eHNP (0, 1, 10 and 100 μg/mL) for 16 h before exposure to TNF- α (50 ng/mL) to maximize inhibition of ICAM-1 expression [30]. During TNF- α activation for 4 h, the concentration of eHNP was maintained. The devices were then fixed and stained for ICAM-1 expression before comparing the fluorescence intensity between the eHNP dosages with confocal microscopy. The fluorescence intensities were normalized to the 0 µg/mL eHNP dosage. ICAM-1 expression without TNF- α was quantified in the same way with the exclusion of the TNF- α incubation step.

4.12. Immunostaining in microengineered vascular system

For immunofluorescence staining, cells in the device were fixed using 4% PFA for 15 min at room temperature (RT), permeabilized with Triton X-100 (0.15% v/v in PBS) for 15 min, and then blocked in bovine serum albumin (BSA 3% w/v in PBS) for 1 h at room temperature. Monoclonal antibodies specific for human ZO-1 (Alexa Fluor 488) were purchased from Thermo Fisher, CD31 (Alexa Fluor 647) were purchased from BioLegend and Hoechst 3342 were purchased from Molecular Probes. Mouse monoclonal antibodies specific for ICAM-1 (Alexa Fluor 488) were purchased from BioLegend. All the samples were washed three times and stored in PBS before imaging.

4.13. Cell viability assay

Trypan blue was used to evaluate the viability of HL-60 cells counted in a Countess II FL Auto from Life Technologies. Cells were cultured at 37 °C in complete medium with Iscove's Modified Dulbecco's Medium and 20% FBS in a 96 well at a density of 20,000 cells/well. Viability was measured in triplicate every 24 h after addition of eHNPs and DOX at a dosage of 150 ng. The amount of eHNPs to be administered to achieve the appropriate DOX dosage was determined through the characterization of DOX loading into the eHNPs (Fig. S7). All measurements were normalized to HL-60 cell samples cultured without the addition of eHNPs or DOX.

4.14. Co-localization of eHNPs and DOX

eHNPs were synthesized using a rhodamine-DMPE lipid to allow for visualization of both eHNPs and DOX. HL-60 cells were incubated with either eHNP-r4F-DOX or eHNP-A1-DOX for 4 h before being fixed for 15 min with 4% PFA at RT and spun onto poly-l-lysine coated glass coverslips and mounted to glass slides using VectaShield (Vector Laboratories, Burlingame, CA) with DAPI counterstain prior to fluorescent imaging with a LSM 700 confocal microscope from ZEISS (Oberkochen, Germany) [52,53]. Images were pseudo-colored for consistency through the study; green for eHNPs, red for DOX, and blue for DAPI.

4.15. Murine xenograft tumor biodistribution of eHNPs

Nude female balb/c mice were ordered at 5 weeks of age and allowed to acclimate to the lab facility conditions for 1 week on an irradiated dietary regiment. Two million HL-60 cells were injected in 100 µL of PBS into the rear right flank of the mouse. To maximize the amount of DOX delivered by the IVIS-trackable eHNPs. increasing amounts of DOX were added to the hydrophobic precursor with DiR to find an upper limit of loaded DOX. Using the 5:1 mass ratio between DOX and protein, a 200 µL tail vein injection of saline, DOX, eHNP-A1-DOX, or eHNP-r4F-DOX was administered to the mouse after its tumor reached at least 100 mm³ in volume as measured by digital calipers (Fig. S8). The dosages for the injections were 5 mg/kg of protein, equivalent to 0.25 mg/kg of DOX. The animals were sacrificed and perfused with saline and 4% PFA for 15 min at RT 24 h after the tail-vein injection to allow for uptake of the eHNPs (12 h half-life for both) into the tumor [14,54]. This 24 h time point was also consistent with the in vitro cytotoxicity assay. The harvested organs were then imaged for their DiR content using an in vivo imaging system (IVIS) from Perkin Elmer (Waltham, MA) (Fig. S9). The organ masses were measured on a scale, and the biodistribution data was calculated from the IVIS data (Fig. S10). The tumors were first cryosectioned and mounted onto glass slides using the antifade mounting medium with DAPI (H-1200) from Vector Laboratories (Burlingame, CA) before being imaged under a confocal microscope (Zeiss LSM 780) [55]. Image analysis of the tumors was done using ImageI for 3 sections per tumor.

4.16. Statistical analysis

Statistical analyses were run in Prism 7 (GraphPad Software Inc, La Jolla, CA) and significance was defined as P < 0.05 (*). Statistical significance analysis was done via t tests or ANOVA.

Competing financial interests

The authors declare no competing financial interests.

Author contributions

Y.J.S. and Y.K. conceived and initiated the entire study. T.K. executed the molecular dynamics simulations. Y.J.S. executed the computational fluid dynamics simulations. Y.J.S., J.A., and A.J.S.L. conducted the *in vitro* experiments. Y.J.S. and E.S. conducted the *in vivo* experiments. S.S.J. and Y.K. supervised the molecular dynamics simulations. N.L.J. and Y.K. supervised the microvasculature experiments. Y.C.J. and Y.K. supervised the *in vivo* experiments. Y.K. supervised all aspects of this study.

Acknowledgments

This work was supported by the National Institutes of Health Director's New Innovator Award 1DP2HL142050 (Y.K.), the American Heart Association Scientist Development Grant 15SDG25080314 (Y.K.), the National Science Foundation CAREER 1653006 (Y.K.), the Center for Pediatric Nanomedicine (CPN) of Children's Healthcare of Atlanta Seed Grant (Y.K.), the Basic Science Research Program through the National Research Foundation of Korea funded by the Ministry of Science, ICT & Future Planning NRF-2015R1A2A1A09005662, 2016R1A4A1010796 (N.L.J.), the National Institutes of Health/National Institute of General Medical Sciences-sponsored Cell and Tissue Engineering (CTEng) Biotechnology Training Program (T32GM008433), and the National Science Foundation Graduate Research Fellowship (DGE-1148903). This work was in part performed at the core facilities at the Parker

H. Petit Institute for Bioengineering and Bioscience at the Georgia Institute of Technology and the Institute for Electronics and Nanotechnology at the Georgia Institute of Technology, a member of the National Nanotechnology Coordinated Infrastructure, which is supported by the National Science Foundation (ECCS-1542174).

Appendix A. Supplementary data

Supplementary data related to this article can be found at https://doi.org/10.1016/j.biomaterials.2018.04.011.

References

- A. Kratzer, H. Giral, U. Landmesser, High-density lipoproteins as modulators of endothelial cell functions: alterations in patients with coronary artery disease, Cardiovasc. Res. 103 (3) (2014) 350–361.
- [2] C. Rohrl, H. Stangl, HDL endocytosis and resecretion, Biochim. Biophys. Acta 1831 (11) (2013) 1626–1633.
- [3] B. Lou, X.-L.L. Liao, M.-P.P. Wu, P.-F.F. Cheng, C.-Y.Y. Yin, Z. Fei, High-density lipoprotein as a potential carrier for delivery of a lipophilic antitumoral drug into hepatoma cells, World J. Gastroenterol. WJG 11 (7) (2005) 954–959.
- [4] B.L. Sanchez-Gaytan, F. Fay, M.E. Lobatto, J. Tang, M. Ouimet, Y. Kim, S.E. van der Staay, S.M. van Rijs, B. Priem, L. Zhang, E.A. Fisher, K.J. Moore, R. Langer, Z.A. Fayad, W.J. Mulder, HDL-mimetic PLGA nanoparticle to target atherosclerosis plaque macrophages, Bioconjugate Chem. 26 (3) (2015) 443–451.
- [5] C.E. Matz, A. Jonas, Micellar complexes of human apolipoprotein A-I with phosphatidylcholines and cholesterol prepared from cholate-lipid dispersions, J. Biol. Chem. 257 (8) (1982) 4535–4540.
- [6] Y. Kim, F. Fay, D.P. Cormode, B.L. Sanchez-Gaytan, J. Tang, E.J. Hennessy, M. Ma, K. Moore, O.C. Farokhzad, E.A. Fisher, W.J. Mulder, R. Langer, Z.A. Fayad, Single step reconstitution of multifunctional high-density lipoprotein-derived nanomaterials using microfluidics, ACS Nano 7 (11) (2013) 9975–9983.
- [7] A.Y. Shih, S.G. Sligar, K. Schulten, Maturation of high-density lipoproteins, J. R. Soc. Interface 6 (39) (2009) 863–871.
- [8] F. Gu, M.K. Jones, J. Chen, J.C. Patterson, A. Catte, W.G. Jerome, L. Li, J.P. Segrest, Structures of discoidal high density lipoproteins: a combined computationalexperimental approach, J. Biol. Chem. 285 (7) (2010) 4652–4665.
- [9] M.J. Thomas, S. Bhat, M.G. Sorci-Thomas, Three-dimensional models of HDL apoa-I: implications for its assembly and function, J. Lipid Res. 49 (9) (2008) 1875—1883.
- [10] M. Navab, G.M. Anantharamaiah, S.T. Reddy, Apolipoprotein Al mimetic peptides, Arterioscler. Thromb. Vasc. Biol. (2005).
- [11] S. Marrache, S. Dhar, Biodegradable synthetic high-density lipoprotein nanoparticles for atherosclerosis, Proc. Natl. Acad. Sci. U.S.A. 110 (23) (2013) 9445–9450.
- [12] L.J. Leman, B.E. Maryanoff, M.R. Ghadiri, Molecules that mimic apolipoprotein A-I: potential agents for treating atherosclerosis, J. Med. Chem. 57 (6) (2014) 2169–2196.
- [13] S. Qin, V.S. Kamanna, J.H. Lai, T. Liu, S.H. Ganji, L. Zhang, W.W. Bachovchin, M.L. Kashyap, Reverse D4F, an apolipoprotein-Al mimetic peptide, inhibits atherosclerosis in apoe-null mice, J. Cardiovasc. Pharmacol. Therapeut. 17 (3) (2012) 334–343.
- [14] Z. Zhang, J. Chen, L. Ding, H. Jin, J.F. Lovell, I.R. Corbin, W. Cao, P.-C.C. Lo, M. Yang, M.-S.S. Tsao, Q. Luo, G. Zheng, HDL-mimicking peptide-lipid nanoparticles with improved tumor targeting. Small 6 (3) (2010) 430–437.
- [15] L. Cui, Q. Lin, C.S. Jin, W. Jiang, H. Huang, L. Ding, N. Muhanna, J.C. Irish, F. Wang, J. Chen, G. Zheng, A PEGylation-free biomimetic porphyrin nanoplatform for personalized cancer theranostics, ACS Nano 9 (4) (2015) 4484–4495.
- [16] Z. Zhang, W. Cao, H. Jin, J.F. Lovell, M. Yang, L. Ding, J. Chen, I. Corbin, Q. Luo, G. Zheng, Biomimetic nanocarrier for direct cytosolic drug delivery, Angew Chem. Int. Ed. Engl. 48 (48) (2009) 9171–9175.
- [17] B.Y. Kim, J.T. Rutka, W.C. Chan, Nanomedicine, N. Engl. J. Med. 363 (25) (2010) 2434–2443.
- [18] Y. Kim, B. Lee Chung, M. Ma, W.J. Mulder, Z.A. Fayad, O.C. Farokhzad, R. Langer, Mass production and size control of lipid-polymer hybrid nanoparticles through controlled microvortices, Nano Lett. 12 (7) (2012) 3587–3591.
- [19] Y. Sei, K. Justus, P. LeDuc, Y. Kim, Engineering living systems on chips: from cells to human on chips, Microfluid. Nanofluidics (2014).
- [20] J.P. Morgan, P.F. Delnero, Y. Zheng, S.S. Verbridge, J. Chen, M. Craven, N. Choi, A. Diaz-Santana, P. Kermani, B. Hempstead, Formation of microvascular networks in vitro, Nat. Protoc. 8 (9) (2013) 1820–1836.
- [21] S. Kim, H. Lee, M. Chung, N.L. Jeon, Engineering of functional, perfusable 3D microvascular networks on a chip, Lab a Chip 13 (8) (2013) 1489–1500.
- [22] J. Ahn, Y.J. Sei, N.L. Jeon, Y. Kim, Probing the effect of bioinspired nanomaterials on angiogenic sprouting using a microengineered vascular system, IEEE Trans. Nanotechnol. PP 99 (2017), 1–1.
- [23] C. Besler, T.F. Luscher, U. Landmesser, Molecular mechanisms of vascular effects of high-density lipoprotein: alterations in cardiovascular disease, EMBO Mol. Med. 4 (4) (2012) 251–268.
- [24] L. Zhang, H. Tong, M. Garewal, G. Ren, Optimized Negative-staining Electron

- Microscopy for Lipoprotein Studies, Optimized negative-staining electron microscopy for lipoprotein studies, 2013.
- A. Kontush, S. Chantepie, M.J. Chapman, Small, dense HDL particles exert potent protection of atherogenic LDL against oxidative stress, Arterioscler. Thromb. Vasc. Biol. 23 (10) (2003) 1881–1888.
- [26] S.M. Gordon, H. Li, X. Zhu, A.S. Shah, L.J. Lu, W.S. Davidson, A comparison of the mouse and human lipoproteome: suitability of the mouse model for studies of human lipoproteins, J. Proteome Res. 14 (6) (2015) 2686–2695.
- E. Scarselli, H. Ansuini, R. Cerino, R.M. Roccasecca, S. Acali, G. Filocamo, C. Traboni, A. Nicosia, R. Cortese, A. Vitelli, The human scavenger receptor class B type I is a novel candidate receptor for the hepatitis C virus, EMBO I, 21 (19) (2002) 5017–5025.
- [28] L. Rohrer, P.M. Ohnsorg, M. Lehner, F. Landolt, F. Rinninger, A. von Eckardstein, High-density linoprotein transport through aortic endothelial cells involves scavenger receptor Bi and atp-binding cassette transporter G1, Circ. Res. 104 (10) (2009) 1142-1150.
- [29] P. Xia, M.A. Vadas, K.-A. Rye, P.J. Barter, J.R. Gamble, High density lipoproteins (HDL) interrupt the sphingosine kinase signaling pathway a possible mechanism for protection against atherosclerosis by HDL, J. Biol. Chem. 274 (46) (1999) 33143-33147.
- [30] M.A. Clay, D.H. Pyle, K.-A. Rye, M.A. Vadas, J.R. Gamble, P.J. Barter, Time sequence of the inhibition of endothelial adhesion molecule expression by reconstituted high density lipoproteins, Atherosclerosis 157 (1) (2001) 23–29.
- L. Fotis, G. Agrogiannis, I.S. Vlachos, A. Pantopoulou, A. Margoni, M. Kostaki, C. Verikokos, D. Tzivras, D.P. Mikhailidis, D. Perrea, Intercellular adhesion molecule (ICAM)-1 and vascular cell adhesion molecule (VCAM)-1 at the early stages of atherosclerosis in a rat model, In Vivo 26 (2) (2012) 243-250.
- [32] P.L. van Haelst, B. Schot, E.S. Hoendermis, M.P. van den Berg, Acute myeloid leukaemia as a cause of acute ischaemic heart disease, Neth. Heart J. 14 (2) (2006) 62-65.
- B. Denard, C. Lee, J. Ye, Doxorubicin blocks proliferation of cancer cells through proteolytic activation of CREB3L1, Elife 1 (2012), e00090.
- V.A. Sardao, P.J. Oliveira, J. Holy, C.R. Oliveira, K.B. Wallace, Morphological alterations induced by doxorubicin on H9c2 myoblasts: nuclear, mitochondrial, and cytoskeletal targets, Cell Biol. Toxicol. 25 (3) (2009) 227-243.
- N. Nishida, H. Yano, T. Nishida, T. Kamura, M. Kojiro, Angiogenesis in cancer,
- Vasc. Health Risk Manag. 2 (3) (2006) 213–219.

 [36] V.G. Oehler, K.Y. Yeung, Y.E. Choi, R.E. Bumgarner, A.E. Raftery, J.P. Radich, The derivation of diagnostic markers of chronic myeloid leukemia progression from microarray data, Blood 114 (15) (2009) 3292-3298.
- D. Van Der Spoel, E. Lindahl, B. Hess, G. Groenhof, A.E. Mark, H.J. Berendsen, Gromacs: fast, flexible, and free, J. Comput. Chem. 26 (16) (2005) 1701-1718.
- [38] S.J. Marrink, H.J. Risselada, S. Yefimov, D.P. Tieleman, A.H. de Vries, The martini force field: coarse grained model for biomolecular simulations, J. Phys. Chem. B 111 (27) (2007) 7812-7824.
- [39] X. Periole, M. Cavalli, S.J. Marrink, M.A. Ceruso, Combining an elastic network with a coarse-grained molecular force field: structure, dynamics, and intermolecular recognition, J. Chem. Theor. Comput. 5 (9) (2009) 2531-2543.
- [40] T.A. Wassenaar, H.I. Ingolfsson, R.A. Bockmann, D.P. Tieleman, S.J. Marrink,

- Computational lipidomics with insane: a versatile tool for generating custom membranes for molecular simulations, J. Chem. Theor. Comput. 11 (5) (2015) 2144-2155
- [41] S.R. Midtgaard, M.C. Pedersen, I.I. Kirkensgaard, K.K. Sorensen, K. Mortensen, K.J. Jensen, L. Arleth, Self-assembling peptides form nanodiscs that stabilize Membrane proteins, Soft Matter 10 (5) (2014) 738–752.
- V.K. Mishra, M.N. Palgunachari, R. Krishna, J. Glushka, J.P. Segrest, G.M. Anantharamaiah, Effect of leucine to phenylalanine substitution on the nonpolar face of a class a amphipathic helical peptide on its interaction with high resolution solution nmr studies of 4f-dimyristoylphosphatidylcholine discoidal complex, I. Biol. Chem. 283 (49) (2008) 34393-34402.
- [43] Y. Kim, S.D. Joshi, L.A. Davidson, P.R. LeDuc, W.C. Messner, Dynamic control of 3D chemical profiles with a single 2D microfluidic platform, Lab a Chip 11 (13) (2011) 2182-2188.
- Y. Kim. K. Pekkan, W.C. Messner, P.R. Leduc, Three-dimensional chemical profile manipulation using two-dimensional autonomous microfluidic control, J. Am. Chem. Soc. 132 (4) (2010) 1339–1347.
- L. Capretto, W. Cheng, M. Hill, X. Zhang, Micromixing within microfluidic devices, Top. Curr. Chem. (2011).
- [46] M.J. Toth, T. Kim, Y. Kim, Robust manufacturing of lipid-polymer nanoparticles through feedback control of parallelized swirling microvortices. Lab a Chip 17 (16) (2017) 2805–2813.
- [47] D. Genovese, S. Bonacchi, R. Juris, M. Montalti, L. Prodi, E. Rampazzo, N. Zaccheroni, Prevention of self-quenching in fluorescent silica nanoparticles by efficient energy transfer, Angew Chem. Int. Ed. Engl. 52 (23) (2013) 5965-5968
- [48] P. Mohan, N. Rapoport, Doxorubicin as a molecular nanotheranostic agent: effect of doxorubicin encapsulation in micelles or nanoemulsions on the ultrasound-mediated intracellular delivery and nuclear trafficking, Mol. Pharm, 7 (6) (2010) 1959-1973.
- [49] C. Snider, S. Jayasinghe, K. Hristova, S.H. White, MPEx: a tool for exploring Membrane proteins, Protein Sci. 18 (12) (2009) 2624-2628.
- J. Ahn, Y.J. Sei, N.L. Jeon, Y. Kim, Tumor microenvironment on a chip: the progress and future perspective, Bioengineering 4 (3) (2017).
- S. Kim, M. Chung, N.L. Jeon, Three-dimensional biomimetic model to reconstitute sprouting lymphangiogenesis in vitro, Biomaterials 78 (2016) 115-128
- [52] W. Wang, A. Shao, N. Zhang, J. Fang, J.J. Ruan, B.H. Ruan, Cationic polymethacrylate-modified liposomes significantly enhanced doxorubicin delivery and antitumor activity, Sci. Rep. 7 (2017) 43036.
- [53] W.L. Ye, J.B. Du, B.L. Zhang, R. Na, Y.F. Song, Q.B. Mei, M.G. Zhao, S.Y. Zhou, Cellular uptake and antitumor activity of DOX-hyd-PEG-FA nanoparticles, PLoS One 9 (5) (2014), e97358.
- R. Kuai, D. Li, Y.E. Chen, J.J. Moon, A. Schwendeman, High-density lipoproteins: nature's multifunctional nanoparticles, ACS Nano 10 (3) (2016) 3015-3041.
- J.Y. Hwang, J. Park, B.J. Kang, D.J. Lubow, D. Chu, D.L. Farkas, K.K. Shung, L.K. Medina-Kauwe, Multimodality imaging in vivo for preclinical assessment of tumor-targeted doxorubicin nanoparticles, PLoS One 7 (4) (2012) e34463.